Available online at www.sciencedirect.com

SciVerse ScienceDirect

Acta Materialia 60 (2012) 2518–2527

Acta MATERIALIA

www.elsevier.com/locate/actamat

Three-dimensional phase-field simulation of micropore formation during solidification: Morphological analysis and pinching effect

H. Meidani [a,*], J.-L. Desbiolles [a], A. Jacot [a,b], M. Rappaz [a]

[a] Computational Materials Laboratory, Institute of Materials, Ecole Polytechnique Fédérale de Lausanne, 1015 Lausanne, Switzerland
[b] Calcom ESI SA, Parc Scientifique, PSE-A, 1015 Lausanne, Switzerland

Received 22 December 2011; accepted 29 December 2011
Available online 14 March 2012

Abstract

A three-dimensional (3-D) multiphase-field model has been developed in order to study the formation of a micropore constrained to grow in a solid network (i.e. pinching effect). The model accounts for the pressure difference due to capillarity between liquid and gas, the equilibrium condition at triple (solid–liquid–pore) lines, and the partitioning and diffusion of dissolved gases such as hydrogen. From the predicted 3-D morphology of the pore, entities such as the interfacial shape distribution are plotted and analyzed. It is shown that the mean curvature of the pore–liquid surface, and thus also the pressure inside the pore, is uniform. The results are then compared with analytical pinching models. While predicting a similar trend, analytical models tend to underestimate the pore curvature at high solid fractions. Despite the complex morphology of pores reconstructed using high-resolution X-ray tomography, the present phase-field results suggest that a simple pinching model based on a spherical tip growing in between remaining liquid channels is a fairly good approximation.

Keywords: Casting defects; Porosity; Solidification microstructure; Simulation; Phase field modeling

1. Introduction

Shape casting processes offer the great advantage of producing complex components in one single production step. However, they are also limited by the formation of defects such as microporosity and hot tearing. Microporosity is a major defect encountered in solidification processes and considerably decreases the mechanical properties of a cast part, namely fatigue life, ductility and tensile strength [1].

Micropores are induced by both solidification shrinkage and gas segregation, which occur concomitantly during the formation of the solid in the mushy zone. In order to better characterize and more importantly minimize this defect, a considerable effort has been dedicated to the modeling of pore formation. These models, which range from very simple criteria functions [2] to sophisticated computational solutions of conservation and state equations, provide quantitative information on the effect of the processing conditions and alloy chemistry on microporosity [3–10].

Among the first models of pore formation, the works of Walter et al. [11] and Piwonka and Flemings [12] should be mentioned. These authors assumed a Hagen–Poiseuille laminar flow of the melt in between solid channels to calculate analytically the pressure drop associated with solidification shrinkage. Later on, more mature models were proposed and the effect of dissolved gas species, with the assumption of very fast diffusion, was successfully accounted for in shrinkage-driven pressure drop calculations in the mushy zone [3,4]. While being capable of explaining many phenomena involved in pore formation, these approaches could not yet explain effects such as the decrease of gas porosity with an increased cooling rate.

* Corresponding author.
E-mail address: hossein.meidani@a3.epfl.ch (H. Meidani).

1359-6454/$36.00 © 2012 Acta Materialia Inc. Published by Elsevier Ltd. All rights reserved.
doi:10.1016/j.actamat.2011.12.049

Based on their experimental X-ray temperature gradient stage observations, Lee and Hunt [5,6] concluded that the pressure drop has a minor effect on pore formation in Al–Cu alloys with a fairly high copper content (>10 wt.%), i.e. high eutectic fraction. They proposed a pore growth model based on the finite-rate diffusion of hydrogen, a concept that was further developed by Atwood et al. [7,8] and applied to Al–Si alloys. A more comprehensive model accounting for both finite-rate hydrogen diffusion and limited flow in the mushy zone of aluminum alloys was proposed recently by Carlson et al. [9].

Common to most advanced models of microporosity formation at the process scale is the consideration of average conservation equations for: (i) the evolution of the solid fraction (microsegregation model and thermal model); (ii) the interdendritic liquid flow to compensate solidification shrinkage (Darcy's equation); (iii) the partitioning and diffusion of gases during solidification; (iv) the formation of pores by nucleation and growth when the local gas composition exceeds their temperature- and pressure-dependent solubility limit. Besides nucleation, this last step is delicate as the actual pressure in the pore exceeds that of the liquid due to capillarity. Thus, to close the problem mathematically, a constitutive model for the radius of curvature of the pore as a function of its volume is required [4,10,13,14]. If the pore is assumed to be spherical, this relationship is straightforward. However, in reality the growth of micropores is limited by the well-developed solid network. Due to numerous contacts with the solid phase, pores take a complex and highly tortuous shape. Local mean curvatures as high as $0.2\,\mu m^{-1}$ have been measured recently in aluminum alloys by X-ray tomography [15,16], which indicates that the pressure difference between the pore and the surrounding liquid can be as high as 400 kPa. Since the pore is a compressible phase, this directly affects the pore size and volume fraction. For such situations, a so-called pinching model, i.e. a mathematical expression relating the radius of curvature of the pore–liquid interface[1] to the volume fraction of solid g_s, microstructural parameters and possibly the volume fraction of pores, g_p, is required.

Different pinching models have been proposed. Initial models assumed that the pore is spherical, with a radius equal to half the dendritic arms spacing, λ_2 [10]. The more elaborate model of Pequet et al. [4] considers different stages: an initial stage during which the nucleated pore "escapes" its foreign substrate with a constant radius; a second stage where the pore is a growing sphere until, third stage, it is pinched by the solid and its radius is given by a function of g_s and λ_2; and finally, a constant radius when some interdendritic eutectic forms near the end of solidification. Poirier et al. [14] assumed the pores to be constrained by dendritic arms arranged in a hexagonal network, and introduced the effect of arms impingement into their model. Couturier and Rappaz [13] refined this model by assuming the pore to grow in between a regular arrangement of spherical grains (in three dimensions) or cylindrical dendrite arms (in two dimensions). The pores grow with an initial spherical shape, until they come into contact with the solid phase: their radius of curvature is then assumed to be given by the largest sphere (three dimensions) or cylinder (two dimensions) that can fit in between the grains, respectively. In other words, they do not change their topology and are never growing in between the solid.

A common point between these models is the simplified pore geometry. However, in reality, the pores have a much more complex shape. A phase-field (PhF) model, directly describing the pore morphology as a function of different parameters such as gas concentration, solid fraction and capillary forces, was presented in Ref. [17], but it was limited to two dimensions. In the present contribution, the model is extended first to three dimensions and validated. In order to overcome the high computational cost, a parallel computer program in C programming language was developed. Finally, the model is used to study the pinching effect in three dimensions and to compare the results with those of analytical (geometrical) models in order to improve the latter.

2. Model

A multiphase-field model is used in this study. Three phase-field variables, $\phi_i(\boldsymbol{x},t)$, where $i = s,\ l,\ p$ is a phase index, are introduced to show the distribution of the solid, liquid and pore, respectively, in time and space. These variables can be understood as local volume fractions and thus linked together using the constraint $\phi_s + \phi_l + \phi_p = 1$. One salient feature of the PhF method is a smooth and continuous variation of ϕ_i across the interfaces [18].

In the present contribution, we adopt the multi-PhF formulation first outlined by Steinbach et al. [19], with the introduction of a Lagrange multiplier Λ to account for the constraint above [20]. More details about the model can be found in Ref. [17]. Spatial and temporal evolution of the phase-field variable ϕ_i is given by the following partial differential equation:

$$\dot{\phi}_i = \sum_{k\neq i} M_{ik}\left[\begin{array}{l}\varepsilon_{ik}^2(\phi_k\nabla^2\phi_i - \phi_i\nabla^2\phi_k) - 2W_{ik}\phi_k^2(1-\phi_k)^2\phi_i(1-\phi_i)(1-2\phi_i)\\ -30\phi_i\phi_k(1-\phi_i)(1-\phi_k)\Delta G_{ik} - \Lambda\end{array}\right] \tag{1}$$

with

$$\Delta G_{sl} = \Delta s_f \Delta T \quad \Delta G_{lp} = p_p - p_l \quad \Delta G_{sp} = 0 \tag{2}$$

and

$$W_{ik} = \frac{15\sqrt{2}\gamma_{ik}}{\delta_{ik}} \quad \varepsilon_{ik}^2 = 2W_{ik}\delta_{ik}^2 \quad M_{ik} = \frac{\mu_{ik}}{\delta_{ik}} \tag{3}$$

[1] Since pressure differences within a pore and outside the surrounding liquid are equalized at the speed of sound in each phase, a quasi-static approximation of the pore–liquid equilibrium implies that the mean curvature at any point of the gas–liquid interface is uniform at any instant.

Here, Δs_f is the volumetric entropy of melting, ΔT is the undercooling, p_p and p_l are the pressures in the pore and in the liquid, respectively, and ε_{ik}^2, M_{ik} and W_{ik} are the three PhF parameters associated with the physical parameters γ_{ik}, μ_{ik} and δ_{ik} describing the interfacial energy, the mobility and the interface thickness, respectively, between phases i and k [18].

The effect of radius of the curvature of the pore is taken into account through the driving force term, for the liquid/pore transformation. It is expressed here as the pressure difference between the pore and the liquid, which can be justified by solving the steady-state form of Eq. (1) in spherical coordinates, for a single pore surrounded by liquid. Doing so, the Laplace pressure condition is recovered:

$$p_p - p_l = 2\gamma_{lp}H \tag{4}$$

where H is the mean curvature of the pore. For a spherical pore of radius r_p, $H = r_p^{-1}$.

Throughout this paper, for the sake of simplicity, we will focus on aluminum alloys, where hydrogen is known to be the gas responsible for pore formation [16]. However, the model is more general and can be applied to any alloy system in which a compressible phase forms. A local volumetric molar concentration of hydrogen, based on averaging procedure, can be introduced as follows:

$$\langle c^H \rangle = \phi_s c_s^H + \phi_l c_l^H + \phi_p c_p^H \tag{5}$$

where c_s^H, c_l^H and c_p^H are volumetric molar concentrations of hydrogen in the solid, liquid and gas, respectively.

The equilibrium solubility of hydrogen in the solid, c_s^H, and liquid, c_l^H, can be expressed as a function of p_p using Sievert's law, while assuming thermodynamical equilibrium at the interface:

$$c_s^H = S_s\sqrt{\frac{p_p}{p_0}} \qquad c_l^H = S_l\sqrt{\frac{p_p}{p_0}} \tag{6}$$

where S_s and S_l are Sievert's constants (in $\text{mole}_\text{H}\ \text{m}^{-3}$) for the solid and liquid, respectively, and p_0 is the standard pressure. Combining Eqs. (5) and (6) and using the perfect gas law gives:

$$\langle c^H \rangle = (\phi_l S_l + \phi_s S_s)\sqrt{\frac{p_p}{p_0}} + \phi_p \frac{2p_p}{RT} \tag{7}$$

Based on the experimental observations of Lee et al. [6,8], the finite rate of hydrogen diffusion in the liquid is assumed to govern the growth kinetics of the pore[2]. This has been taken into account in the model through a hydrogen conservation equation, neglecting any hydrogen concentration gradient in the gas phase and any hydrogen transport in the liquid due to convection:

$$\frac{\partial \langle c^H \rangle}{\partial t} = \nabla \cdot (\phi_s D_s^H \nabla c_s^H + \phi_l D_l^H \nabla c_l^H) \tag{8}$$

A finite volume method with an explicit time-discretization scheme is used to numerically solve Eqs. (1) and (8). At each time step, the phase distribution is calculated by solving Eq. (1); then, Eq. (8) is solved to calculate the concentration field. Besides, the calculation of the driving force terms of Eq. (1) requires solving the second order polynomial expression of Eq. (7) to obtain p_p from $\langle c^H \rangle$. Since homogenization of the hydrogen concentration inside the pore is assumed to be infinitely fast (uniform p_p), the average hydrogen concentration inside the pore, $\bar{c}_p^H$, is calculated over all the mesh points of the pore (i.e. for which $\phi_p > 0$) and is then applied to all these points.

For the diffusion and phase equations, no flux boundary conditions are used. Therefore, the number of moles of hydrogen remains constant in the domain. In the meantime, due to the large density difference between the gas and the condensed phase, the mass is not conserved and thus the hydrogen content per unit mass (e.g. $cc_{STP}/100_{gr,Al}$) varies over time. The hydrogen content per unit mass corresponding to a set of simulation conditions can only be determined once equilibrium has been reached, and assuming a certain value for the pore number density, n_p.

Besides, due to the high computational cost of the three-dimensional (3-D) PhF calculations, the simulation domain is much smaller than the volume associated with one pore, i.e. n_p^{-1}. Calculations were therefore undertaken at relatively large hydrogen contents (or supersaturation) in order to compensate for this effect. In other words, the calculation domain is a small window centered on one pore, which is a particular area of the microstructure where the hydrogen content is locally high. This causes another difficulty in analyzing the effect of hydrogen content and pore growth kinetics. As the present 3-D model is an extension of the previously published two-dimensional (2-D) model [17], the reader is referred to this publication for more details.

It should be pointed out that, in the present calculations, the repartition of the solid phase was prescribed and fixed at the beginning of the computation, i.e. the evolution equation for ϕ_s was not solved, in order to isolate and analyze the pinching effect only.

3. Analysis of pore curvature

Characterization of the pore–liquid interface in three dimensions requires computing its curvature in order to better understand the pinching effect. A procedure similar to that used by Felberbaum et al. [16] for the analysis of the curvature of pores reconstructed in three dimensions using X-ray tomography was employed. It is recalled that, for any surface patch, two principal radii of curvature, r_{p1} and r_{p2}, can be defined, from which two principal curvatures, $\kappa_1 = r_{p1}^{-1}$ and $\kappa_2 = r_{p2}^{-1}$, can be obtained. The local mean curvature, H, is then given by:

[2] It should be noted that, besides solidification shrinkage which is accounted here through the local pressure p_l, the growth of the pore can also be limited by the viscosity of the fluid. Such is, for example, the case of bubbles formed during cavitation. This contribution is neglected here through the quasi-static approximation.

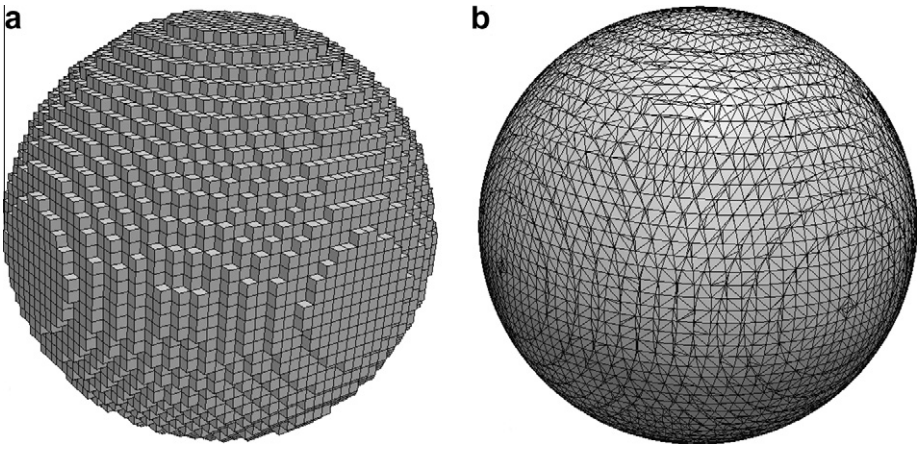

Fig. 1. 3-D volume rendering of a spherical pore made up of voxels (the resolution has been reduced for graphical resons). (a) Threshold representation for $\phi_p \geqslant 0.5$. (b) The triangular mesh of the fitted surface.

$$H = \frac{(\kappa_1 + \kappa_2)}{2} \tag{9}$$

For the problem at hand, the pore–solid interface (when $\phi_l = 0$) is simply deduced from the prescribed shape of the solid and thus is known. For the complex pore–liquid interface, such is not the case and thus the iso-surface of the pore–liquid interface corresponding to $\phi_p = \phi_l = 0.5$ (i.e. $\phi_s = 0$) was extracted from the 3-D reconstruction of the results. Note that the diffuse triple line characterized by the region where ($\phi_s \neq 0$ and $\phi_p \neq 0$ and $\phi_l \neq 0$) is not considered in the present analysis. However, it was checked in a similar manner as in 2-D PhF simulations that the Young–Laplace equation is satisfied at such locations [17]. Then, the surface given by all the mesh points (or voxels in X-ray tomography) where $\phi_p = \phi_l = 0.5$ was smoothed by triangular elements using the Avizo software (Avizo is a registered trade mark of Mercury Computer Systems, Chelmsford, Massachusetts). As can be seen in Fig. 1, the size of the triangular elements is close to the mesh size. For each of the triangles composing this surface, a quadratic surface was then fitted considering a certain number (n_n) of triangular neighbors. Since curvature corresponds to first derivatives of the unit surface normal along principal curvature directions [21], or second derivatives of the surface positions, using nearest-neighbor triangles alone is not accurate enough. On the other hand, large values of n_n increase the calculation time and also result in a loss of accuracy by excessive smoothing of the surface. The best tradeoff between accuracy and performance was achieved with $n_n = 18$, while analyzing the curvature of a reference sphere. Since the size of the triangles is close to the mesh size Δx, $18\Delta x$ must be compared with the radius r_p of the sphere ($r_p \cong 200\ \Delta x$) and with the thickness w_{ik}[3] of the diffuse interface ($w_{ik} \cong 15\ \Delta x$).

[3] The thickness w_{ik} of the interface is defined here as the width along the gradient of the phase over which the phase ϕ_i or ϕ_j itself changes from 0.05 to 0.95. With the model used here, $w_{ik} = 66\ \delta_{ik}$.

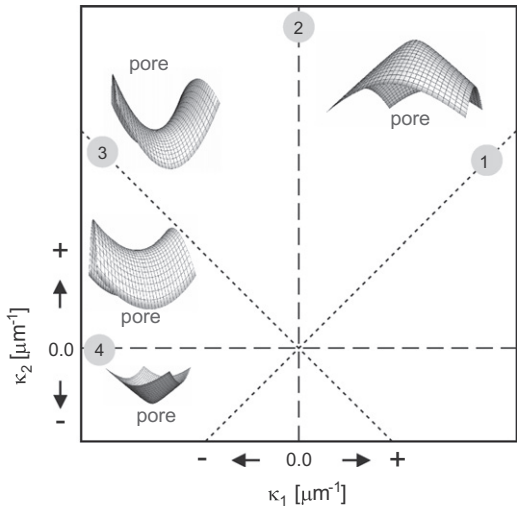

Fig. 2. κ_1–κ_2 space used to draw the ISD plot $P(\kappa_1,\kappa_2)$, representing the probability of having a surface element of the pore interface with the curvature (κ_1,κ_2). The curvature is measured with a unit surface normal pointing out of the pore.

Pores in three dimensions can have a very complex morphology, as shown recently by Felberbaum et al. using X-ray tomography [16]. Yet, at any instant during growth, the pore–liquid interface must have a uniform mean curvature in order to have a uniform gas pressure p_p. This leaves nevertheless one degree of freedom, i.e. if p_p (or H) is fixed, once one of the principal curvatures at a given point of this interface is given, say κ_1, the other one is known. For such 3-D situations, a useful tool for a detailed analysis of the pore morphology based on both κ_1 and κ_2 is the interfacial shape distribution (ISD) plot, first introduced by the group of Voorhees and coworkers for the analysis of coarsening of dendritic structures [22]. The ISD is a 2-D probability contour plot, $P(\kappa_1,\kappa_2)$, which measures the probability of having a surface patch, i.e. a triangular element in this case, with its principal curvatures falling in the range ($\kappa_1 - \Delta\kappa/2$, $\kappa_1 + \Delta\kappa/2$) and ($\kappa_2 - \Delta\kappa/2$, $\kappa_2 + \Delta\kappa/2$). Note that the areas of the triangular elements at which the curvatures are

Table 1
Parameters used in the PhF calculations.

Parameter	Unit	Numerical value	Ref.
Mesh size	m	5.0×10^{-8}	
δ_{ik}	m	1.2×10^{-8}	
p_l	Pa	10^5 Pa	
T	K	1000	
μ_{ik}	$m^3\ J^{-1}\ s^{-1}$	1×10^{-6}	
D_l	$m^2\ s^{-1}$	1×10^{-6}	
S_l	$mol_H\ m^{-3}$	0.69	
γ_{pl}	$J\ m^{-2}$	0.9	[23]
γ_{ps}	$J\ m^{-2}$	1.1	[24]
γ_{ls}	$J\ m^{-2}$	0.15	[25]

estimated are taken into account in the statistics. By definition, the curvatures are selected such that $\kappa_2 \geqslant \kappa_1$. The distribution $P(\kappa_1,\kappa_2)$ is then plotted in a (κ_1, κ_2) diagram in the form of isovalues. By definition, the distribution can have non-zero values only above the line $\kappa_2 = \kappa_1$, and several regions can be distinguished in Fig. 2. They are separated by various lines: (1) points on the line $\kappa_2 = \kappa_1$ correspond to pore–liquid surface elements having locally a spherical topology which can be convex ($H > 0$) or concave ($H < 0$); (2) points along the line $\kappa_1 = 0$ ($\kappa_2 > 0$) correspond to pore elements with a convex cylindrical topology; (3) along the line $\kappa_2 = -\kappa_1$, the pore surface has a saddle shape with a zero mean curvature; (4) along the line $\kappa_2 = 0$ ($\kappa_1 < 0$), the pore surface element has also a cylindrical topology, but concave. In between these lines, a few morphologies have been illustrated.

4. Results and discussion

4.1. Model validation

In order to validate the model, the simple case of a pore growing freely into a liquid without a constraint imposed by the solid is first considered. In this case, the equilibrium size of the spherical pore can be calculated analytically once the domain size, initial hydrogen concentration (c_0^H), hydrogen solubility, liquid pressure, interfacial energies and temperature are specified. This is achieved by using the Laplace–Young equation (Eq. (4)), Sievert's law (Eq. (6)), the perfect gas law ($p_p = 0.5 c_p^H RT$) and the following hydrogen mass balance over the computational domain:

$$V_p c_p^H + (V_{comp} - V_p) c_l^H = V_{comp} c_0^H \tag{10}$$

where V_{comp} is the volume of the computational domain and $V_p = 4/3\pi r_p{}^3$ is the pore volume.

The PhF calculations were performed in a cubic domain of edge $2a = 25.6\ \mu m$, containing a supersaturated liquid ($c_0^H = 15\ mol_H m^{-3}$, note that $1\ mol_H\ m^{-3} = 0.5\ mol_{H_2}\ m^{-3}$). A small spherical pore was set at the center of the domain and the calculations were performed using the parameters listed in Table 1.

The evolutions of the volume V_p and pressure p_p of the pore calculated with the model are compared with the analytical solution in Fig. 3. As can be seen, both converge towards the analytical solution after a short transient state, the final volume of the pore being $\sim 3400\ \mu m^3$, i.e. $r_p = 9.3\ \mu m$. This shows the ability of the model to correctly predict the final state of a pore in equilibrium with its surrounding liquid. In the present situation, the transient is dictated by the diffusion of hydrogen alone. Taking half the edge of the cube, i.e. $a = 12.8\ \mu m$, the typical diffusion time of hydrogen in the liquid is given by $(a^2/D_l) = 1.6 \times 10^{-4}$ s, a time scale that is on the order of the transient time seen in Fig. 3.[4] Once complete mixing of hydrogen is achieved in the liquid, the pore stops growing.

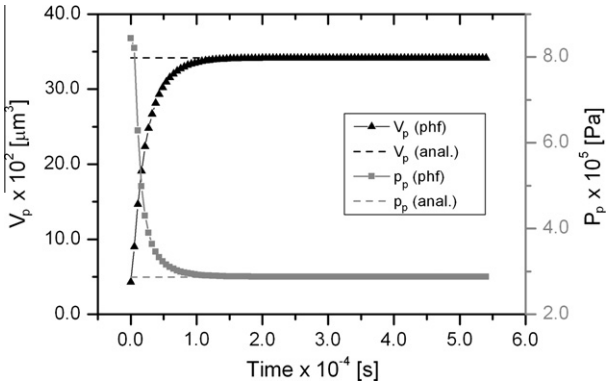

Fig. 3. Evolutions of the pressure p_p and volume V_p of the pore calculated with the PhF model (solid lines) and compared with the analytical solution (dashed lines).

Two phenomena have been neglected in the present situation, both related to the movement of the liquid. The first one is associated with the transport of hydrogen due to convection, which modifies the solute profile in the liquid. Indeed, the Péclet number, $Pe_p = (r_p v_p)/D_l$ associated with the radius r_p and the velocity $v_p = dr_p/dt$ of the pore–liquid interface is ~2. This shows that advection cannot be neglected. The second contribution is directly linked with the dynamic pressure in the liquid, i.e. the viscous forces needed to push the liquid away, which is proportional to ($\mu_l\ v_p/r_p$). However, this last contribution is only on the order of 10 Pa, i.e. a value much smaller than the capillary pressure $2\gamma_{pl}/r_p \cong 200$ kPa. In actual situation where the density of pores is typically $10^{-9}\ m^3$, diffusion (and partitioning) of hydrogen at the scale of a domain typically 1 mm in size will be the dominant contribution to the transient anyway.

The distribution of the mean curvature estimated from the calculated spherical pore is illustrated in Fig. 4. It is in good agreement with the analytical solution ($H = 0.107\ \mu m^{-1}$) and the value calculated using the Laplace–Young equation (Eq. (4)). Fitting a Gaussian distribution to the distribution gives $H = 0.108\ \mu m^{-1}$, with a full width at half maximum $FWHM = 0.006\ \mu m^{-1}$, a broadening of ~6% of the curvature estimation.

[4] One could have taken the distance separating the pore–liquid interface from the edge of the volume, (a–r_p), to have a better estimate).

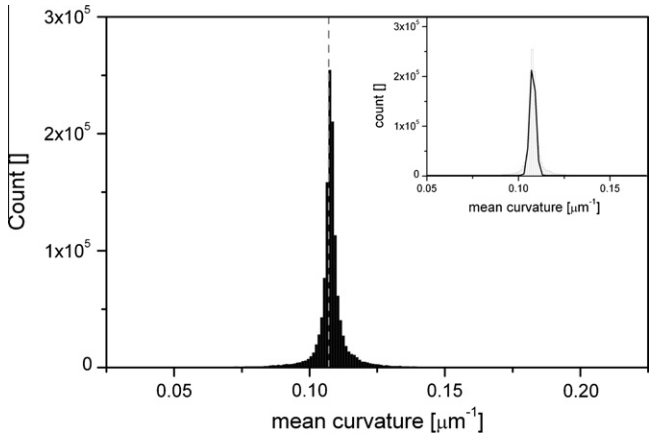

Fig. 4. Measured local mean curvature distribution compared with the analytical solution (vertical dashed line). The inset shows the Gaussian fitting on the distribution.

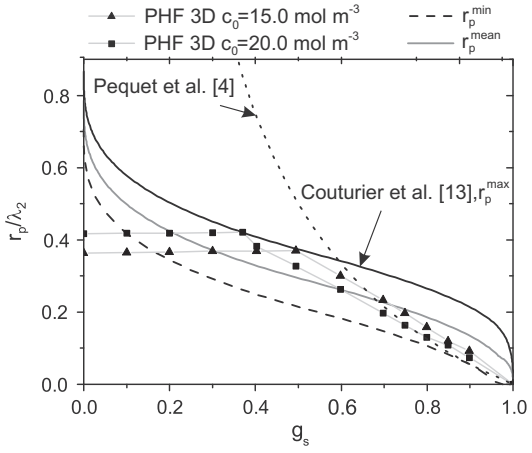

Fig. 6. Normalized mean radius of curvature of the pore, $r_p = H^{-1}$, plotted as a function of the volume fraction of solid, calculated with the 3-D PhF model and the analytical models of [4,13].

4.2. Comparison with analytical pore pinching models

Conceptually, the present porosity model can be applied to any complex geometrical situation such as a representative volume element (RVE) obtained from X-ray microtomography [16]. However, because of the heavy computation time inherent to the PhF method and also because it is interesting to compare the present results with analytical models of pinching [4,13], simple situations are first considered here.

A simplified solid morphology, similar to the 3-D model of Couturier et al. [13], was selected. In this configuration, eight solid grains are placed in a cubic arrangement (inset in Fig. 5). Different solid fractions were obtained by simply changing the radius, r_s, of the solid grains. During the calculations, r_s remains constant, i.e. the evolution of the grains is neglected. For each solid fraction, a small spherical pore is nucleated at the center of the octahedral space. Since the liquid is initially supersaturated in hydrogen, the pore grows, initially as a sphere, with a decreasing mean curvature. Once the pore comes into contact with the solid, it has to grow in the narrow liquid channels left between the grains and thus the curvature of the pore–liquid interface increases. It grows until equilibrium is reached, i.e. until the hydrogen content in the liquid is uniform and corresponds to the solubility limit of the final pressure p_p within the pore (Eq. (6)). Such a pore grown at $g_s = 0.7$ ($r_s = 14.3\ \mu$m for a cube edge $\lambda_2 = 25.6\ \mu$m[5]) and $c_0^H = 20\ \mathrm{mol_H\ m^{-3}}$ is illustrated in Fig. 5. The different color patches in this figure indicate the local mean curvature. Areas with negative mean curvature (blue patches) are in contact with the solid and thus are characterized by a mean curvature $H_{ps} = -r_s^{-1} = -0.07\ \mu\mathrm{m}^{-1}$. The main area of interest is the pore–liquid interface where the mean curvature is positive (red patches). This positive curvature is linked to the pressure difference between the pore and the liquid through the Laplace–Young equation (Eq. (4)). Since p_p and p_l are homogenous, the mean curvature of the pore–liquid interface is also expected to be constant over the pore–liquid interface, which is the case here as shown by the uniform red color. The calculated mean curvature for the pore shown in this figure, $H = 0.198\ \mu\mathrm{m}^{-1}$, is in good agreement with that obtained from the pressure difference (p_p–p_l) extracted from the PhF calculations and Eq. (4) ($H = 0.193\ \mu\mathrm{m}^{-1}$).

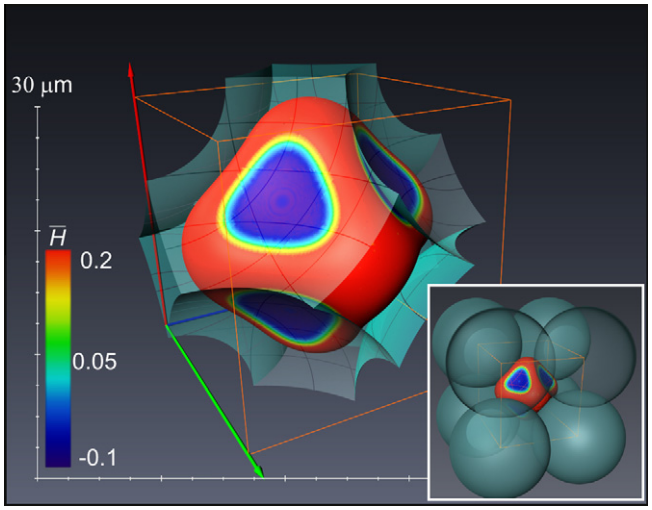

Fig. 5. The morphology of a pore, grown at $g_s = 0.7$ and $c_0^H = 20\ \mathrm{mol_H\ m^{-3}}$. The color of the pore shows the local mean curvature which has been calculated on the surface patches. The solid surface in contact with the pore is indicated by transparent surface (cadet blue). The insert shows the pore surrounded by the eight spherical solid grains.

For each solid fraction, a different calculation was performed and the steady state mean curvature, H, of the pore–liquid interface was calculated using the (p_p–p_l) value extracted at the end of the PhF calculation. These values were also compared with those deduced from the mean curvature directly calculated from the pore geometry. Per-

[5] Although λ_2 usually refers to the secondary arm spacing of dendritic specimens, it is used here to be similar to the notation used by Couturier et al. for both dendritic and globular specimens.

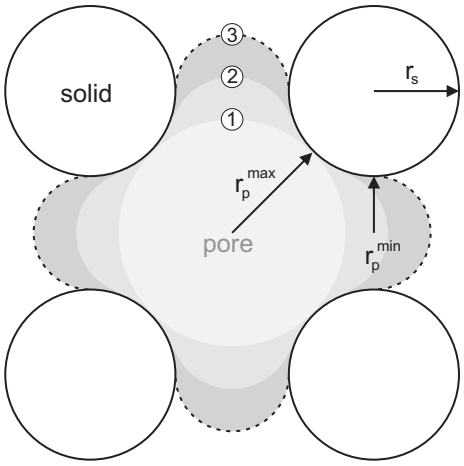

Fig. 7. 2-D sketch of the three possible conditions for a pore, constrained by cylindrical solid particles arranged in a cubic network. Pores 1, 2 and 3 correspond to the maximum, intermediate and minimum possible radius of curvature of the pore in this condition, respectively.

forming a series of calculations for different solid fractions, it is possible to plot the mean radius of curvature $r_p = \mathrm{H}^{-1}$ as a function of g_s. The PhF results for two different initial hydrogen concentrations, $c_0^H = 15$ and $20\ \mathrm{mol_H\ m^{-3}}$, are shown in Fig. 6 with triangle and square symbols, respectively. The radius, r_p, has been normalized by the distance between the grains, λ_2, and is compared with the analytical curves of Couturier in 3-D (solid black lines) [13], and Pequet [4] (short dashed line).

Before making any meaningful comparison between pinching models, we should first keep in mind that not all the range of g_s, i.e. from 0 to 1, has to be considered in practice for pore formation. It is usually assumed that r_p cannot change once the alloy reaches the eutectic composition, which for example occurs between $g_s = 0.5$ and $g_s = 0.8$ for A356 aluminum alloys [9]. On the other hand, pores usually do not form (and thus are not pinched) when $g_s < 0.4$–0.5 if humidity, and thus the hydrogen content, is controlled. These two values specify the region of interest for the pinching models.

In Fig. 6, at low solid fractions, i.e. small r_s, the final pore shape is still spherical for both compositions, since it is not pinched. The pore radius increases only slightly with g_s as a result of the increased partitioning of hydrogen into the liquid due to an increased solid fraction. At a certain value of g_s, the final pore comes into contact with the solid, i.e. this occurs when $2(r_s + r_p) = \sqrt{3}\lambda_2$. This corresponds precisely to the intersection of the points/curve calculated with the PhF model and the curve of Couturier. For a higher nominal composition c_0^H, this point moves to lower values of g_s. Beyond this critical value, pinching starts and the pore grows with a reduced mean radius of curvature r_p (or increased mean curvature H) in the liquid channels left between the grains. At the beginning of pinching, the PhF results are closer to, but always lower than, the curve of Couturier et al. [13]. As g_s further increases, the results get closer to the curve of Pequet et al. [4].

Considering now physically the growth of a pore for a fixed value of r_s and λ_2 (and g_s), the maximum radius of a spherical pore is given by the model of Couturier, i.e. $r_p^{\max} = (\sqrt{3}/2)\lambda_2 - r_s$ (the conversion of r_s into g_s is straightforward up to $r_s = \lambda_2/\sqrt{2}$ and requires a few geometrical calculations above this limit, when the solid grains impinge on each other). In this model, the radius of curvature of the pore is independent of the pore fraction, or of the hydrogen composition, c_o^H. However, as this composition increases, the pore can be pushed in between the solid grains, as shown schematically in Fig. 7 for a 2-D situation. In other words, for a given value of r_s and λ_2, the model of Couturier defines a maximum radius of curvature $r_p^{\max}$, but a minimum radius of curvature, $r_p^{\min}$ can also be defined: it corresponds to the smallest space left in between two solid grains (dashed line in Fig. 6). Indeed, in a previous contribution, we have shown that the radius of curvature of the pore is bound between two limits that are dictated by the solid morphology, namely the liquid channel widths [17]. Increasing c_0^H for a given microstructure makes r_p increase up to $r_p^{\max}$ in a first step (spherical pore), then decrease up to $r_p^{\min}$ (pinching of the pore), the point at which the pore can suddenly expand into a neighboring space, and goes back to a value close to $r_p^{\max}$.

In 3-D, the radius $r_p^{\min}$ is given by the circle that can be inscribed in between the solid spheres in any face of the cubic RVE. It is thus given by $\left(\frac{\lambda_2}{\sqrt{2}} - r_s\right)$ up to $g_s = 0.965$. The curve $r_p^{\min}(g_s)$ is also shown in Fig. 6 as a lower bound.

As can be seen, the PhF results show that once the spherical pore comes into contact with the upper curve $r_p^{\max}$ given by Couturier's model, its radius of curvature decreases and finally reaches the curve $r_p^{\min}$ when it passes the middle of the channel between four solid grains. Considering a distribution of liquid channel widths in a casting, it sounds reasonable to define a mean value $r_p^{mean} = (r_p^{\min} + r_p^{\max})/2$ for a pinching effect that could be used in macroscopic porosity models.

4.3. Pore morphology analysis

ISD plots corresponding to the pore presented in Fig. 5 are plotted in Fig. 8a, taking into account its entire interface, and in Fig. 8b for its interface in contact with the liquid only. Both figures exhibit a set of points aligned along a diagonal line $(\kappa_1 + \kappa_2) = cst$, in the area where the mean curvature of the pore is positive. Extracting the pressure difference $(p_p$–$p_l)$ from the PhF results to calculate the mean curvature of the interface ($H = 0.193\ \mu\mathrm{m}^{-1}$, Eq. (4)) gives the black dashed line shown in Fig. 8b. As can be seen, this line matches very well the principal curvature values (κ_1, κ_2) calculated at various points of the pore–liquid interface. The maximum density of these points in Fig. 8b furthermore corresponds to the nearly spherical "tip" of the pore located in between four grains, close to the faces of the RVE, for which $\kappa_1 = \kappa_2$ (see Fig. 4). But the points in the ISD plot also extend toward the line

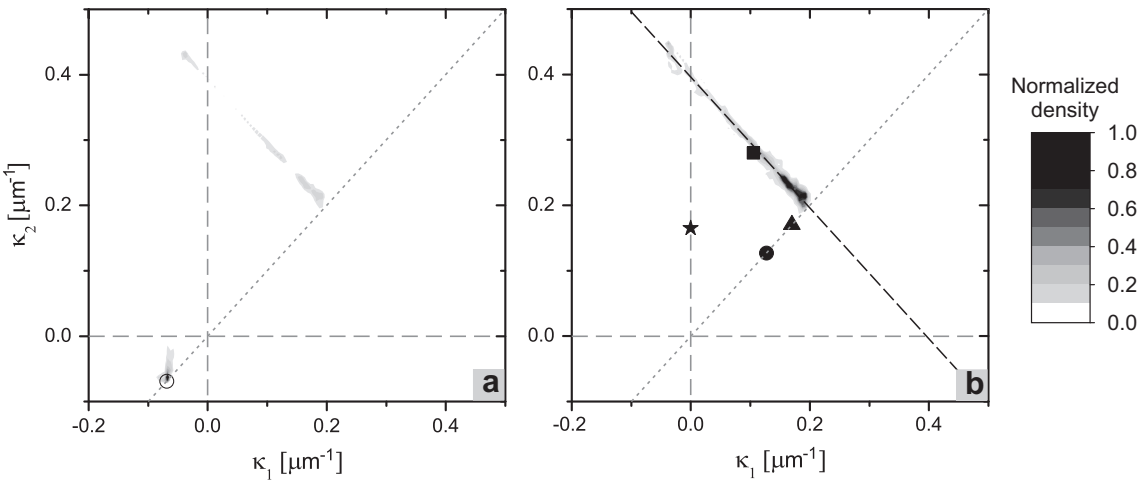

Fig. 8. ISD plots corresponding to the pore presented in Fig. 5, taking into account the entire pore interface (a), and the interface with liquid only (b). The empty circle represents the curvature corresponding to a pore surface in contact with the spherical solid phase, while the black square indicates the average mean curvature measured on the pore–liquid interface. The triangle, black sphere and the star indicate the curvature given by the r_p^{mean} line and 3-D and 2-D model of Couturier, respectively.

$\kappa_1 = 0$, i.e. $\kappa_2 = 2H$, which corresponds to the cylindrical-type shape of the pore located in between two grains (see Fig. 5). The fact that all the surface elements of the pore–liquid interface are along this line $(\kappa_1 + \kappa_2) = 2H = 0.386$ ensures that the pressure within the pore is indeed uniform. The mean values $((\bar{\kappa}_1, \bar{\kappa}_2)$ averaged over the entire pore–liquid interface are shown with a black square.

The predictions of the 2-D and 3-D models of Couturier [13] are also presented in Fig. 8b with a black star and circle, respectively. The PhF model predicts a higher mean curvature value compared to these models, in agreement with the previous discussion related to $r_p^{\max}$ (prediction of Couturier), $r_p^{\min}$ and r_p^{mean}. It is to be noted that Felberbaum et al. [15] also measured a higher mean pore curvature in Al–Cu alloys, compared to the model of Ref. [13].

In Fig. 8a, another set of points can be seen at negative values of κ_1, more specifically at $\kappa_1 = -0.07\ \mu m^{-1}$ and for $-0.07\ \mu m^{-1} < \kappa_2$. These points correspond to the pore–solid interface. Since the pore adopts the shape of the spherical grains, we can expect that $\kappa_1 = \kappa_2 = -r_s^{-1} = -0.07\ \mu m^{-1}$. This is shown with an open circle, which clearly surrounds the maximum of the ISD plot in this region of Fig. 8a. Another feature of Fig. 8a is the transition area between this region of the ISD plot and the previous one associated with the pore–liquid interface. This is due to the fact that the pore surface has been reconstructed using the iso-values $\phi_p = 0.5$. This value corresponds to the middle of a two-phase interface, but this is no longer the case at regions where all three phases coexist. Indeed, at the center of the diffuse triple line where the mechanical equilibrium condition between solid, liquid and pore should hold, one has $\phi_p = 1/3$. Finally, these ISD plots also contain a noise contribution as the curvature is a second derivative of the calculated interfaces.

Based on X-ray microtomography observations of Felberbaum et al. [16], pores have a high density of cylindrical

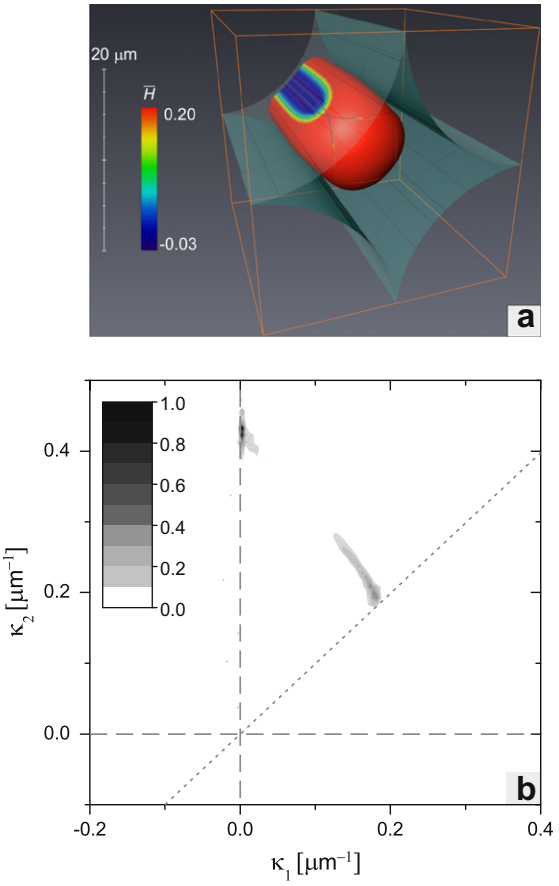

Fig. 9. (a) Morphology of a pore grown at $c_0^H = 10.5\ mol_H\ m^{-3}$, in between cylindrical solid arms having a radius $r_s = 12.8\ \mu m$ and corresponding to $g_s = 0.79$ in the RVE (domain size $\lambda_2 = 25.6\ \mu m$). The color of the pore shows the local mean curvature which has been measured on the surface patches. The solid surface in contact with the pore is indicated by transparent surface (cadet blue). (b) Corresponding ISD plot of the pore–liquid interface only.

surface patches, near the $\kappa_1 = 0$ line, in dendritic specimens. To reproduce such morphology, the situation shown

in Fig. 9 is considered. In this case, four cylindrical and parallel dendrite arms of spacing λ_2 are set up in the RVE, while a pore is nucleated in the middle of one of its faces. The shape of the equilibrium pore with $c_0^H = 10.5\,\mathrm{mol_H\,m^{-3}}$ is shown in Fig. 9a, with a color indicating again the local mean curvature. In the ISD plot corresponding to the pore–liquid interface only (in Fig. 9b), a higher density of points close to the $\kappa_1 = 0$ line can be observed. This reflects the cylindrical-type shape of the pore seen in Fig. 9a. The other points of the pore–liquid interface are spread along a line $(\kappa_1 + \kappa_2) = 2H = cte$, which is expected from the uniform pressure condition imposed for the pore (Eq. (4)). The "tip" of the pore has a spherical shape and corresponds to points in the ISD plot at the intersection of this line with the diagonal $\kappa_1 = \kappa_2$. Note that the second principal curvature $\kappa_2 = 2H$ of the cylindrical surface patch of the pore is twice the equal principal curvatures of the spherical tip.

Comparing now the present situation of Fig. 9 with the model of Couturier for cylindrical dendrite arms, the maximum radius that can fit in between these arms is given by $r_p^{\max} = \left(\frac{\lambda_2}{\sqrt{2}} - r_s\right)$ [13]. However, as the pore can penetrate slightly in between these arms (Fig. 9a), the radius of curvature κ_2^{-1} of these cylindrical surface patches of the pore is smaller than $r_p^{\max}$, as was the case for the previous situation (Fig. 5). Nevertheless, the nearly spherical tip of the pore is almost given by the maximum sphere that can be inscribed between these arms, and so for this part of the pore one has: $\kappa_1 = \kappa_2 \cong (r_p^{\max})^{-1}$. In summary, the 2-D model of Couturier for a dendritic specimen can be reasonably used, but with the mean curvature given by $H = (r_p^{\max})^{-1}$ in Eq. (4) and not $\frac{1}{2}(r_p^{\max})^{-1}$.

In any case, pores growing at high solid fraction will try to follow a path of maximum liquid space, i.e. minimal pore–liquid curvature. Even in a dendritic specimen, such spaces are found near the tips of the dendrites, and not near their roots. For example, in a specimen exhibiting a columnar structure, secondary dendrite arm tips are in a configuration close to that shown in Fig. 5, and not to that of Fig. 9. Therefore, the pinching model with a r_p^{mean} value, equal to $(r_p^{\max} + r_p^{\min})/2$, might actually describe better a dendritic specimen than the curvature of a pore growing in between cylindrical arms (Fig. 9). Yet, Felberbaum et al. [15] found an ISD plot that is essentially cylindrical in nature (i.e. $\kappa_1 = 0, \kappa_2 > 0$), while the PhF simulation of Fig. 5 shows a majority of spherical pore–liquid interface patches. However, it should be kept in mind that the X-ray micro-tomography measurements were made on fully solidified specimens and that all the points measured correspond to the final pore–solid interface. A long pore growing at fairly high solid fraction as a succession of pockets between dendrite tips will exhibit a very small pore–liquid interface, i.e. only a very small fraction of the positively curved pore–solid interface measured in Ref. [16] might actually correspond to the pore–liquid interface calculated here. This clearly shows that in situ, high-resolution X-ray micro-tomography measurements need to be done in the future to actually observe the pinching effect during solidification.

5. Conclusion

A 3-D PhF model, which is capable of describing the complex morphology of pores growing in between a pre-existing solid phase, has been developed. The model accounts for partitioning and diffusion of hydrogen, capillary forces at different interfaces and Laplace–Young's condition. The results show that the presence of the solid affects the pore morphology, which then influences its internal pressure, and thus its total volume. After validating the model for a free spherical pore growing in the liquid, two situations were considered, namely two pores growing in between globular grains and in between cylindrical dendrite arms.

The PhF results were compared with two analytical models of Couturier et al. [13], which describe the pinching effect for similar geometries. For a pore growing between globular grains, it was found that the pore remains spherical up to the value $r_p^{\max}(\lambda_2, g_s)$ given by Couturier's relationship. Then, its radius of curvature decreases as it is forced to penetrate in between the grains up to a minimal radius $r_p^{\min}(\lambda_2, g_s)$ which was derived analytically. If the pore can pass this maximum curvature, it can then grow in a neighbor void and increase again its radius. As there is also a distribution of grain sizes in a real microstructure, we propose then to use a radius r_p^{mean} for predicting the curvature overpressure (Eq. (4)) in macroscopic porosity calculations.

In the present model, the growth kinetics of the pore is supposed to be governed by gas diffusion only. At present, diffusion in the solid is neglected due to its low solubility, but at high solid fraction, this cannot be neglected any more [9,26]. On the other hand, if the growth rate of the pore is high, pushing away the liquid, i.e. viscous term contributions, cannot be neglected either. Finally, although X-ray tomography characterization of as-solidified alloys has shed light on the curvature and complex morphology of pores, in situ measurements during solidification should be made to further validate the present PhF results. Thanks to the advances in ultra-fast tomography techniques and the development of furnaces that can fit X-ray beam lines [26], this should be possible in the near future.

Acknowledgments

The authors would like to thank the Swiss Competence Centre for Materials Science and Technology (CCMX) and partner companies, Asulab, Constellium, Kugler Bimetal, Novelis, Rolex and Varinor, within the thematic area "Multi-scale, multi-phenomena modeling of metallic systems" for funding this research.

References

[1] Dantzig JA, Rappaz M. Solidification. Lausanne: EPFL Press; 2009.
[2] Niyama E, Uchida T, Morikawa M, Saito S. Int Cast Met J 1982;7:52.
[3] Sabau A, Viswanathan S. Met Trans 2002;33 B:243.
[4] Pequet C, Rappaz M, Gremaud M. Metall Mater Trans A 2002;33:2095.
[5] Lee PD, Hunt JD. In: Cross M, Campbell J, editors. Conference on modeling of casting, welding and advanced solidification processes VII. Warrendale, PA: TMS; 1995. p. 585.
[6] Lee PD, Hunt JD. Acta Mater 1997;45:4155.
[7] Atwood R, Lee P. Metall Mater Trans B 2002;33:209.
[8] Atwood RC, Sridhar S, Zhang W, Lee PD. Acta Mater 2000;48:405.
[9] Carlson KD, Lin Z, Beckermann C. Metall Mater Trans A 2007;38:541.
[10] Kubo K, Pehlke R. Metall Mater Trans B 1985;16:359.
[11] Walther WD, Adams CM, Taylor HF. AFS Trans 1956:64.
[12] Piwonka TS, Flemings MC. Trans AIME 1966;236:1157.
[13] Couturier G, Rappaz M. Light metals. San Antonio, TX: TMS; 2006. p. 143.
[14] Poirier DR, Yeum K, Maples AL. Metall Mater Trans A 1987;18:1979.
[15] Felberbaum M. PhD thesis. EPFL Lausanne; 2010.
[16] Felberbaum M, Rappaz M. Acta Mater 2011;59:6849.
[17] Meidani H, Jacot A. Acta Mater 2011;59:3032.
[18] Boettinger WJ, Warren JA, Beckermann C, Karma A. Ann Rev Mater Res 2003;32:163.
[19] Steinbach I, Pezzolla F, Nestler B, Seeßelberg M, Prieler R, Schmitz GJ, et al. Physica D: Nonlinear Phenomena 1996;94:135.
[20] Nestler B, Wheeler AA. Physica D: Nonlinear Phenomena 2000;138:114.
[21] Pressley A. Elementary differential geometry. New York: Springer; 2001.
[22] Mendoza R, Alkemper J, Voorhees P. Metall Mater Trans A 2003;34:481.
[23] Hatch JE. Aluminum: properties and physical metallurgy; 1984.
[24] Kumikov VK, Khokonov KB. J Appl Phys 1983;54:1346.
[25] Morris JR. Phys Rev B 2002;66:144104.
[26] Fife J, Rappaz M, Pistone M, Celcer T, Mikuljana C, Stampanoni M. J Synchlotron Radiat, submitted.